Consistency Analysis of RTK and Non-RTK UAV DSMs in Vegetated Areas

Umut Gunes Sefercik and Mertcan Nazar

Abstract—Lately, unmanned aerial vehicles (UAVs) evolve into one of the most popular remote sensing technologies by providing rapid and periodical acquisition of high-resolution, accurate, and low-cost aerial data. Progressively, the technology of UAVs rises with the addition of advanced equipment such as multispectral (MS) digital cameras and global navigation satellite system (GNSS) receivers with real-time kinematic (RTK) positioning ability. While MS cameras aid to achieve higher land use and land cover classification accuracy, RTK GNSS receivers provide real-time positioning without the need for ground control points (GCPs), reducing fieldwork prior to UAV flights. In this study, the consistency of digital surface models (DSM) produced using RTK and non-RTK UAVs' simultaneously acquired data was evaluated with model-based visual and statistical comparison analysis in a densely vegetated study area. The analysis was done for six different vegetation classes utilizing non-RTK UAV DSM which is GCP-supported and has higher spatial resolution, as the reference model. To determine the effect of terrain inclination, the whole area and uninclined areas (arctan-10.1~6°) were analyzed separately. The visual and statistical outcomes show that the absolute vertical consistency of the DSMs depending on the restricted positioning potential of on-board RTK GNSS receivers in the UAVs is insufficient for particularly high vegetation areas and GCP-supported absolute orientation is required.

Index Terms—Accuracy, consistency, digital surface models (DSM), real-time kinematic (RTK), unmanned aerial vehicles (UAVs).

I. INTRODUCTION

THE history of unmanned aerial vehicles (UAVs) is not as short as it is thought and started in 1783 with the use of hot-air balloons. The time between the first military (1849) and civilian (2006) use is around 160 years [1]. With the production of the first camera-equipped Phantom UAV (Phantom 1) by DJI company in 2013, the scientific and commercial applications were started alongside military purposes [2], [3]. Progressively, the swiftly improving UAV technology has become crucial for mapping, geology, mining, smart agriculture and forestry, architecture, archeology, and virtual and augmented reality applications [4], [5], [6], [7], [8], [9], [10], [11]. The main body, payload capacity, and technological complexity of the UAVs have been continuously improved in accordance with the requirements of the applications. Undoubtedly, the major improvements were realized in spatial and spectral resolution of the obtained data and precise positioning without ground control points (GCP). For acquiring high spatial resolution aerial photos, optical UAV systems are usually outfitted with red-green-blue (RGB) single-band digital cameras. Nevertheless, RGB cameras are not suitable for obtaining spectral reflectance values in various imaging bands especially required in modern digital agriculture and forestry applications. The aforementioned issue is one of the main reasons for multispectral (MS) or hyperspectral digital camera integration into UAV systems. Besides a larger capture interval of electromagnetic energy, MS UAV cameras provide data to use vegetation indices such as normalized difference vegetation index and enhanced vegetation index, significant in many land use and land cover applications [12], [13]. For the UAV positioning and the automatic alignment of aerial photos, the global navigation satellite system (GNSS) receivers are integrated into the UAVs. Formerly, the positioning accuracy of on-board GNSS receivers was approximately a few meters, and for the aerial photo alignment, GCPs were essential. Lately, thanks to the addition of low-cost real-time kinematic (RTK) GNSS receivers the positioning performance of UAVs are increased in the flights, and time-consuming groundwork because of the establishment of GCPs and terrestrial GNSS measurements was eliminated [14], [15].

All of the novel instruments in the UAV technology independently work with high performance and reduce the workload. However, the spatial resolution of the MS cameras is not as high as the RGB cameras and geometric correction is not GCP-supported in RTK-equipped UAVs. At this point, particularly about imaging geometry, a significant question "What is the positioning performance of the low-cost on-board RTK GNSS receivers in UAVs?" has to be answered. In the literature, due to being an actual topic, the number of investigations is limited. Remzi et al. [16] compared the performances of UAV-RTK and UAV-PPK (post-processing kinematic) techniques in mapping various surface forms and demonstrated that the greatest differences were obtained over trees and shadow areas. Lewicka et al. [17] investigated the positioning performance of RTK GNSS-equipped UAV in two routes with three different speeds and demonstrated the significant difference.

In this study, 3D description and positioning consistency of MS RTK and RGB non-RTK UAV data in vegetated areas were demonstrated by comparing generated digital surface models (DSMs) with model-based visual and statistical approaches. To eliminate the spectral difference between MS and RGB data and
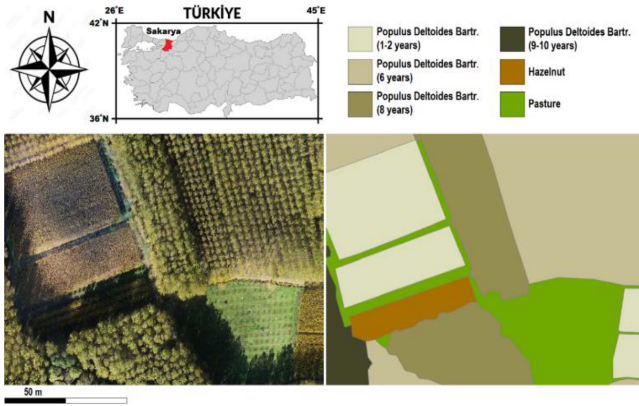
Fig. 1. Study area and existing vegetation classes.

focus on RTK GNSS receiver performance on DSM quality, only the RGB band of MS UAV aerial photos was employed in photogrammetric processing and DSM generation. A DSM is the 3D digital cartographic description of the visible surface of the target region with planimetric coordinates, X and Y, and altitude Z. Distinct from a digital terrain or elevation model (DTM, DEM), which represents only the bare earth surface, it includes the visible surface of all natural and man-made terrain and nonterrain features. A DSM is the first produced 3D product from space-borne and airborne remote sensing systems and the DTM/DEM is generated with filtering of the DSM [18]. The aerial photos were achieved by RTK and non-RTK UAVs' simultaneous flights at the same altitude (90 m). The DSMs were generated in 0.25 m grid spacing and RGB DSM, generated using GCPs, was preferred as the reference model for horizontal and vertical consistency analysis.

II. STUDY AREA AND MATERIALS

The study area is located in Sakarya Province, one of the largest metropolitans in the northwestern region of Türkiye. The area is mainly used for purposes of agriculture and forestry and is dominated by six major vegetation classes as four varied poplar species, hazelnut, and pasture. The orthometric height of the bare ground is approximately 35 m and the high vegetation (∼40 m Populus Deltoides Bartr., 9–10 years) attains up to 75 m. Fig. 1 displays the study area and existing vegetation classes on RGB UAV orthomosaic in high-resolution (20 MP). In the study, for capturing aerial photos, DJI Phantom 4 MS RTK and DJI Phantom 4 Pro V2.0 RGB non-RTK UAVs were utilized. The equipment and the size of these UAVs are almost the same except for the cameras and RTK GNSS receiver. This similarity allows us to prove the pros and cons of the additional equipment. The main specifications of the used UAVs are presented in Table I. GCPs with polycarbonate material and MAPIR Camera Reflectance Calibration Ground Target Package (V2) were used for the 3D orientation and radiometric calibration of the UAV data, respectively. GCP measurements were done using CHC-i80 GNSS receiver. The properties of auxiliary equipment used for 3D orientation and radiometric correction are shown in Table I.

TABLE I
PROPERTIES OF USED EQUIPMENT FOR AERIAL PHOTO ACQUISITION AND
GEOMETRIC AND RADIOMETRIC CORRECTIONS

| Properties	DJI P4 MS	DJI P4 PRO V2	Properties	CHC-i80 – GCP - MAPIR
	Value			**Value**
Camera	6 pieces 1/2.9" CMOS, RGB+5 monochrome, 2.08 MP	1 piece 1" CMOS, RGB 20 MP	GNSS technology	GPS, GLONASS, GALILEO, BeiDou, SBAS, NavIC
Camera focal length	5.7 mm	8.8 mm	Operating system	Linux
Gimbal	3-axis, (pitch, roll, yaw) Vertical: -90° - +30°		Working modes	Static, VRS RTK, UHF RTK, all surveying modes
RTK GNSS receiver	Include	Not include	Positioning accuracy RTK	±0.8 cm H, ±1.5 cm V with initialization reliability >99.9%
Positioning accuracy of RTK GNSS	H: 1 cm + 1 ppm V: 1.5 cm + 1 ppm	-	Modem - Bluetooth	4G, 3G, GSM – V4
Hover accuracy range	RTK: V: ±0.1m, H: ±0.1m Non-RTK: V: ±0.1m, H: ±0.3m (Vision); V: ±0.5m, H: ±1.5m (GPS)	V: ±0.1m, H: ±0.3m (Vision); V: ±0.5m, H: ±1.5m (GPS)	Charge	Dual; Static 10 h Cellular 9h UHF 6h
Max. flight time - Weight	27 min - 1487 gr	27 min - 1375 gr	Network-RTK	Available
Max. velocity	13.8 m/s		Internal memory	32 GB
Max. operational wind speed	10 m/s		GCP	0.25 m × 1 m, polycarbonate
Max. operational temperature	0°- 40°		Radiometric calibration panel	MAPIR Calibration Ground Target Package (V2)
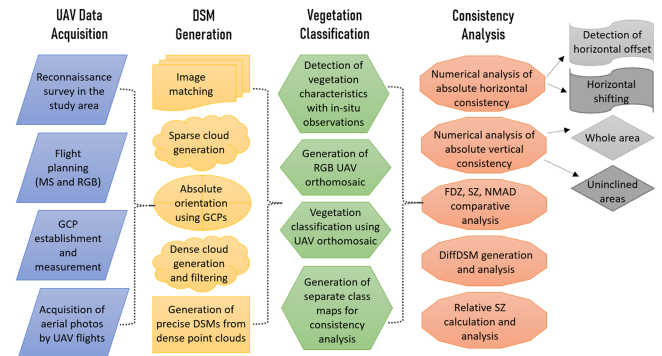
Fig. 2. Methodology workflow.

III. METHODOLOGY

The methodology includes four major stages: UAV data acquisition, generation of the DSMs, vegetation classification, and consistency analysis between the DSMs (see Fig. 2). Considering the requirement of high resolution for vegetation modeling, UAV flights were organized in double-grid geometry applying 90 m altitude. With the advantage of double-grid missions, vegetation was observed from four sides as North-South and East-West, and 3D modeling performance was considerably increased [19], [20]. Since the tall poplar trees obscure the shorter ones in oblique shooting, the nadir camera view was preferred instead of the oblique view in the flights. Moreover, by applying a nadir camera view in UAV flights, the influence of forest geometry on interpolation was decreased to a degree reducing the chance of both obtaining an insufficient number of points under forest canopy and gaps and holes appearing in

Fig. 3. Distribution of established GCPs over the study area.

TABLE II
PRECISION OF USED GCPS

GCP	X (m)	Y (m)	Z (m)	RMSE (m)	Mean RMSE (m)
1	545340.392	4506344.137	37.679	0.020	
2	545360.119	4506346.208	37.738	0.022	
3	545374.112	4506341.507	37.819	0.013	
4	545389.312	4506346.670	37.986	0.013	0.016
5	545388.006	4506331.200	37.956	0.015	
6	545383.297	4506320.772	37.949	0.008	
7	545367.741	4506313.861	37.961	0.012	
8	545349.077	4506331.693	37.751	0.019	

TABLE III
ACCURACY OF THE GENERAL MODEL AFTER ABSOLUTE ORIENTATION

GCP/ ICP	X (m)	Y (m)	Z (m)	RMSE (m)	Mean RMSE (m) 5 GCPs	3 ICPs
1	545340.392	4506344.137	37.679	0.111		
2	545360.119	4506346.208	37.738	0.022		
3	545374.112	4506341.507	37.819	0.013		
4	545389.312	4506346.670	37.986	0.034		
5	545388.006	4506331.200	37.956	0.015	0.016	0.068
6	545383.297	4506320.772	37.949	0.008		
7	545367.741	4506313.861	37.961	0.018		
8	545349.077	4506331.693	37.751	0.019		

output orthomosaic. In the flights, the minimum front overlap ratio was preferred as 80% and the side overlap was 60% to improve the performance of 3D modeling. Finally, the aerial photos were achieved with 2.23 and 4.86 cm ground sampling distance (GSD) from RGB and MS RTK UAV sequentially. Although the camera spatial resolutions of RGB UAV and MS RTK UAV are 20 and 2.08 MP, by means of differences such as focal length, CMOS sensor width, and image size, the GSD of MS RTK UAV's aerial photos is around only half of RGB UAV's and sufficient for 3D detailed representation of terrain and nonterrain objects in the study area.

The photogrammetric processing of the aerial photos was completed by Agisoft Metashape Professional, a Structure from Motion (SfM)-based software. The SfM technique is a low-cost and robust photogrammetric method that offers the ability to reconstruct 3D geometry in high accuracy and high resolution by using a collection of consecutive photos with specific overlap ratios [21], [22]. For geometric corrections, well-representative eight polycarbonate GCPs were established and measured by CHC-i80 GNSS receiver before UAV flights to use in the absolute orientation of the matched aerial photos of the non-RTK UAV (see Fig. 3). The GCPs were established considering some significant criteria as

1) in open areas such as pasture;
2) easily detectable from aerial photos;
3) without shadow effect;
4) not close to tall poplars;
5) to be on the ground.

For MS UAV, due to RTK GNSS contribution, established GCPs were not used for geometric correction. Table II shows the precision of GCPs, used for orientation, as root mean square error (RMSE)

$$\text{RMSE}_{\text{GCP}} = \sqrt{\frac{\sum_{i=1}^{n}\left(\hat{X}_i - X_i\right)^2 + \left(\hat{Y}_i - Y_i\right)^2 + \left(\hat{Z}_i - Z_i\right)^2}{n}} \quad (1)$$

where $\hat{X}_i, \hat{Y}_i, \hat{Z}_i$ = estimated values for i camera position
X_i, Y_i, Z_i = input values for i camera position

As shown in Table II, the mean RMSE of utilized GCPs is 1.6 cm which corresponds to approx. 0.7 pixel. The accuracy of the general model after absolute orientation was validated using 3 of 8 GCPs (1, 4, and 7), all utilized in the orientation, as independent check points (ICP). In contrast to GCPs, ICPs are not used for orientation and determine the difference between reference values, observed by GNSS measurements, and the generated model derived from oriented UAV data. Utilizing ICPs provide a far more objective quantification of the true accuracy of orientation procedures. Considering ICPs, the accuracy of the general model was calculated according to (2)–(5) and the mean RMSE of ICPs was calculated as 6.8 cm which corresponds to three pixels (see Table III) [23], [24], [25]

$$\text{RMSE}_X = \sqrt{\frac{\sum\left(X_{\text{GNSS}} - X_{\text{UAV}}\right)^2}{n}} \quad (2)$$

$$\text{RMSE}_Y = \sqrt{\frac{\sum\left(Y_{\text{GNSS}} - Y_{\text{UAV}}\right)^2}{n}} \quad (3)$$

$$\text{RMSE}_Z = \sqrt{\frac{\sum\left(Z_{\text{GNSS}} - Z_{\text{UAV}}\right)^2}{n}} \quad (4)$$

$$\text{RMSE}_{\text{ICP}} = \sqrt{\text{RMSE}_X^2 + \text{RMSE}_Y^2 + \text{RMSE}_Z^2}. \quad (5)$$

After geometric corrections, a dense point cloud was generated at high-quality level by applying mild depth filtering. Agisoft Metashape Professional has a built-in depth filtering algorithm that assists in eliminating outlier points resulting from images with noise or poor focus. The depth filtering assesses
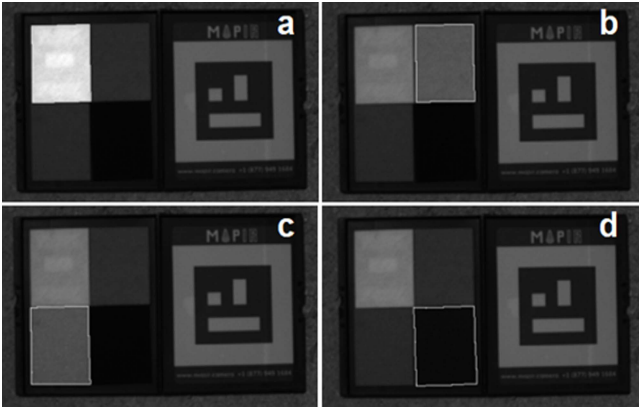
Fig. 4. Masked reflectance targets. (a) White. (b) Light gray. (c) Dark gray. (d) Black.

pairwise depth maps for matched photos utilizing an associated component filter which evaluates the segmented depth maps considering the pixel range from the sensor [26]. The optimal level of depth filtering is very significant in dense cloud generation. If fine details need to be get, mild or moderate depth filtering has to be chosen otherwise aggressive filtering may cut off them as outliers and extraneous points. However, mild or moderate depth filtering is not sufficient to eliminate all of the outlier points, especially have minimum or maximum elevations. Dense point cloud generation with depth filtering is not a short-time process because the generation of depth maps is mandatory to complete it. After dense point clouds were generated by applying depth filtering in Agisoft Metashape, detailed filtering steps were completed in the Microstation software TerraSolid module.

Up to dense point cloud generation, the differences between RGB UAV and MS UAV data processing are the radiometric calibration requirement of MS UAV aerial photos and the direct geometric correction potential of MS UAV by means of RTK GNSS receiver. The radiometry of the aerial photos, obtained in MS imaging bands, was calibrated using reference spectral values, achieved from the MAPIR V2 ground target. The photos of the MAPIR V2, used for radiometric calibration were taken by the MS UAV before the flights. MAPIR V2 has four independent colors white, black, light grey, and dark grey, and their certain spectral reflectance values are provided by the distributor. In the radiometric calibration process, four colors were masked individually to isolate them from the rest for an accurate operation (see Fig. 4) [27]. In this study, due to eliminating spectral difference between MS RTK and RGB non-RTK UAV data and focus on RTK GNSS receiver performance on DSM quality, only the RGB band of MS UAV was calibrated and dense point cloud was generated utilizing only the RGB aerial photos.

In the DSM generation with very high-resolution UAV data, tall objects with vertical geometry such as trees or walls cause a significant problem in high-quality 3D representation. In the calculation of a pixel height in DSM generation, lots of points with different elevations are included. This problem can be solved by applying the value of the highest point instead of averaging [28]. From this point of view, data metrics interpolation method was employed in vector-raster transformation to use the highest

TABLE IV
EFFECT OF FILTERING ON THE NUMBER AND HEIGHT INTERVAL OF GENERATED DENSE POINT CLOUDS

Data source	Number of points before filtering	Number of points after filtering	Height interval before filtering (m)	Height interval after filtering (m)
MS UAV	7780494	7764078	7.36-99.15	35.25-74.15
RGB UAV	48447885	48224438	-9.06-92.96	35.20-74.87

TABLE V
DETECTED AND ELIMINATED HORIZONTAL OFFSET IN X AND Y DIRECTIONS

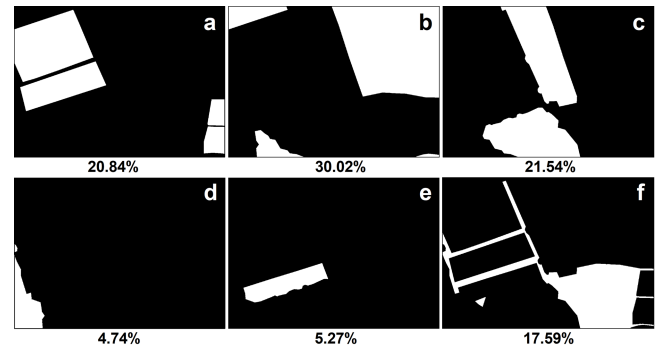| Reference DSM	Shifted DSM	SX (m)	SY (m)
RGB (0.25m)	MS (0.25m)	-0.015 (-0.7 pixel)	0.008 (0.4 pixel)

Fig. 5. Vegetation classes in the study area. (a) Populus Deltoides Bartr. (1–2 years). (b) Populus Deltoides Bartr. (6 years). (c) Populus Deltoides Bartr. (8 years). (d) Populus Deltoides Bartr. (9–10 years). (e) Hazelnut. (f) Pasture.

point value for each pixel rather than more commonly preferred kriging method [29]. The precise DSMs of RGB UAV and MS RTK UAV were generated using Surfer 15 Software in 0.25 m grid spacing.

For consistency validation of generated DSMs, a group of significant pre-processes were performed. First, the Turkish Reference Frame ITRF96 was defined as the coordinate system. The vertical datum was determined as the orthometric height and the geoid undulations, caused by geoid and ellipsoid difference, were eliminated. To achieve correct results from the vertical analysis, 100% horizontal overlap of the compared DSMs is a must. Equation (6) shows the effect of a horizontal offset (DL) in the height discrepancy (DZ) depending upon the terrain inclination (α)

$$DL = \frac{DZ}{\tan(\alpha)}. \qquad (6)$$

To provide 100% overlap of the DSMs, as a second step, the horizontal offset of the DSMs was calculated and eliminated by horizontal shifting utilizing area-based cross-correlation [30]. Subsequently, the vertical consistency was analyzed in six vegetation classes as four poplar classes, hazelnut, and pasture. Fig. 5
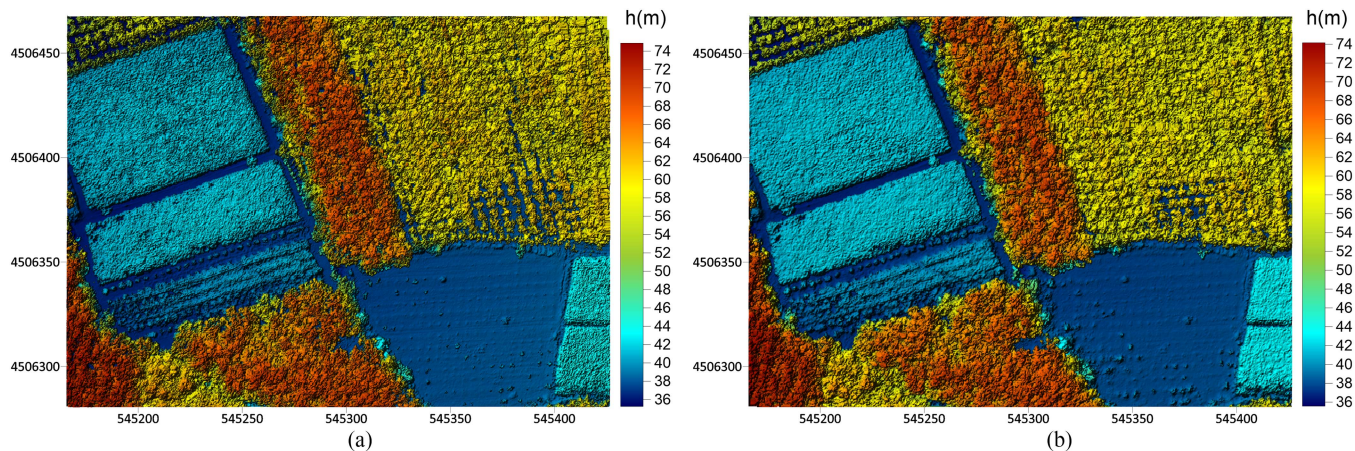
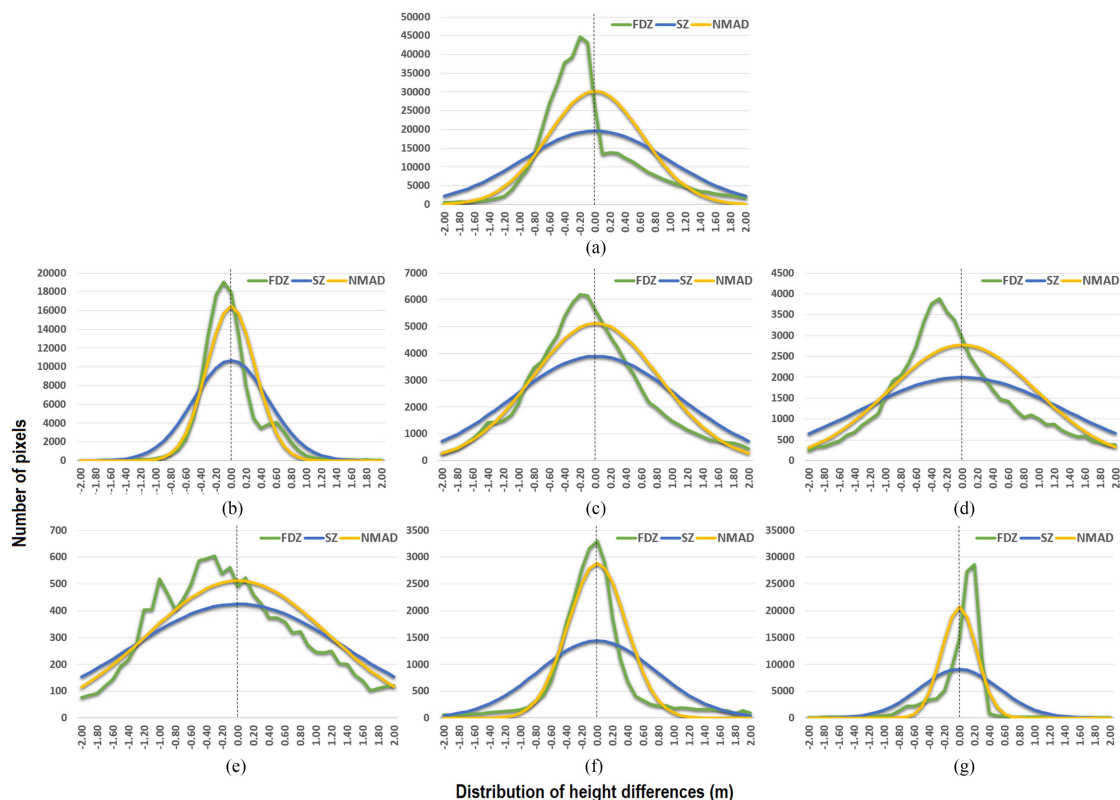Fig. 6.   (a) MS RTK and (b) RGB non-RTK DSMs (0.25 m grid).

Fig. 7.   Height difference distribution histograms. (a) Whole area. (b) Populus Deltoides Bartr. (1–2 years old). (c) Populus Deltoides Bartr. (6 years old). (d) Populus Deltoides Bartr. (8 years old). (e) Populus Deltoides Bartr. (9–10 years old). (f) Hazelnut. (g) Pasture.

shows the existing vegetation classes and their percentage. The vegetation classes were manually vectorized from a 2.5 cm grid RGB UAV orthomosaic in NetCAD software with the help of in-situ observations. The dominancy of the poplar trees in the study area is clear with 89.99%.

The absolute and relative vertical consistencies of MS RTK and RGB non-RTK UAVs' DSMs were analyzed by utilizing BLUH (Bundle Block Adjustment Leibniz University Hannover) and LISA software. In the analysis, the standard deviation (SZ) and the normalized median absolute deviation (NMAD) of

height differences between MS RTK DSM and RGB non-RTK DSM was used as the main consistency estimators (7) and (9). NMAD is a robust estimator to determine major pixel height differences between compared DSMs and the derivative of median absolute deviation (MAD) (8). However, it is not as sensitive as SZ for determining minor height differences [31]. If the height differences are in a normal distribution, identical values of SZ and NMAD are expected. However, particularly in high vegetation areas, inconsistency due to sudden height changes and difficult imaging geometry cause abnormal distributions. In that
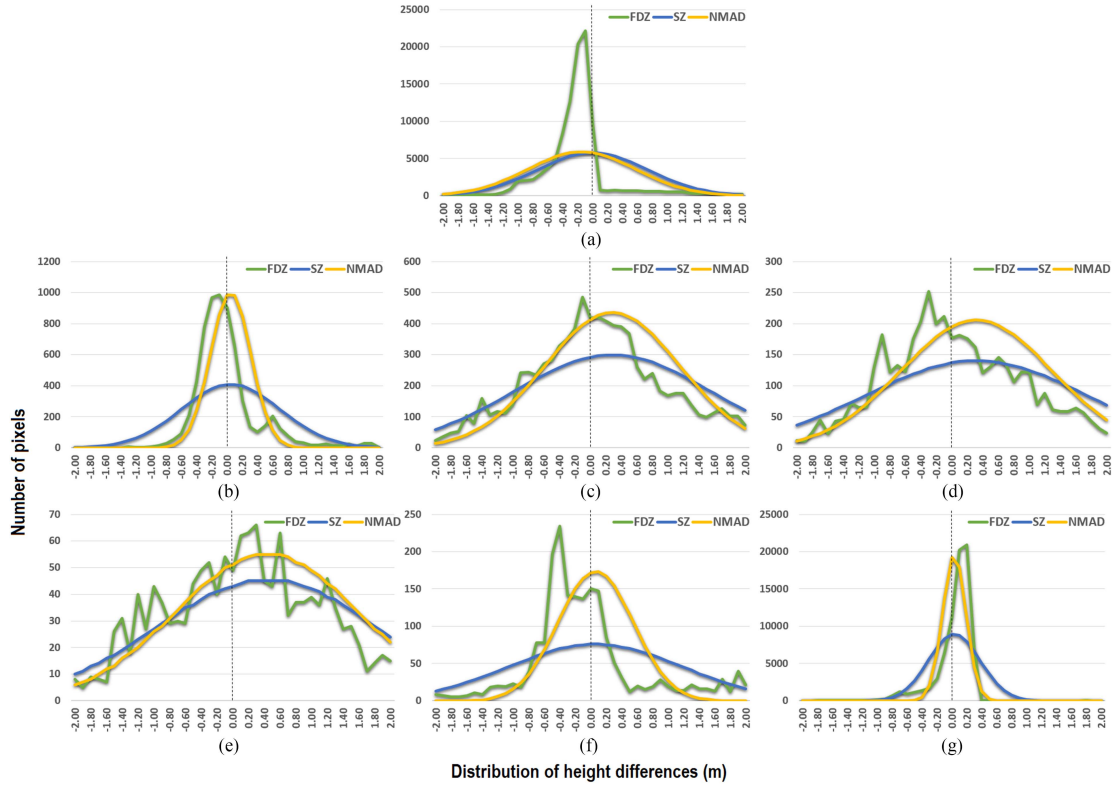
Fig. 8. Height difference distribution histograms in uninclined areas. (a) Whole area. (b) Populus Deltoides Bartr. (1–2 years old). (c) Populus Deltoides Bartr. (6 years old). (d) Populus Deltoides Bartr. (8 years old). (e) Populus Deltoides Bartr. (9–10 years old). (f) Hazelnut. (g) Pasture.

case, the correlation of NMAD and the frequency distribution of height differences (FDZ) is higher than the correlation between SZ and FDZ.

$$\text{SZ} = \sqrt{\frac{\sum_{i=1}^{n}\left(\Delta Z_i - \mu\right)^2}{n-1}} \qquad (7)$$

$$\text{MAD} = \tilde{x}_i\left[|\Delta Z_i - \tilde{x}_j\left(Z_j\right)|\right] \qquad (8)$$

$$\text{NMAD} = 1.4826 * (\text{MAD}) \qquad (9)$$

where n is the compared pixel number in the DSMs; ΔZ is the height differences and μ is the arithmetic mean of the ΔZ (bias). $\tilde{x}_j$ is the median of ΔZ univariate data set (ΔZ_1, ΔZ_2, ΔZ_3, ..., ΔZ_n) and $\tilde{x}_i$ is the median of absolute values of the ΔZ data set from $\tilde{x}_j$. NMAD is obtained with the normalization of MAD with the factor of 1.4826. In reference model-based DSM accuracy and consistency analyses, a height difference limit is set to eliminate the effect of blunder pixels with coarse errors and to avoid misleading results [21]. In these very low number pixels, height differences between reference model and compared model are unusually high due to different facts such as wind-based movements in the forest areas. Height differences in these pixels do not reflect reality and cause misleading results in differential analysis. In the analysis performed for this study, the height difference limit value was determined as ±5 m. By this way, an improvement was achieved in the confidence level of SZ and NMAD, and the pixels which have >5 m height difference

from the reference pixel were defined as the "excluded point" and not included in the consistency analyses.

In the analysis, skewness and kurtosis coefficients were also calculated for better interpretation of the consistency histograms. These indicators are expected around zero if the height difference distribution is normal. The skewness represents the lack of symmetric distribution in the horizontal direction of the histogram. The height distribution that concentrates on the left side of the histogram mode indicates a negative skew coefficient where the right side means positive. Perpendicular to the skewness, kurtosis is the vertical evaluation of the histogram. If the histogram mode is at the upwards of normal distribution mode that means a positive kurtosis and the height differences mostly locate around one value. Vice versa means negative kurtosis. Equations (10) and (11) show the skewness and kurtosis calculations for a univariate data set of height discrepancies (ΔZ_1, ΔZ_2, ΔZ_3, ..., ΔZ_n). In the equations, μ is the arithmetic mean and n is the number of pixels

$$\text{skewness} = \frac{\sum_{i=1}^{n}\frac{(\Delta Z_i - \mu)^3}{n}}{SZ^3} \qquad (10)$$

$$\text{kurtosis} = \frac{\sum_{i=1}^{n}\frac{(\Delta Z_i - \mu)^4}{n}}{SZ^4}. \qquad (11)$$

For visual interpretation of height inconsistency between the DSMs, color-coded differential DSMs (DIFFDSM) were generated with (12). With the advantage of DIFFDSMs, the influence
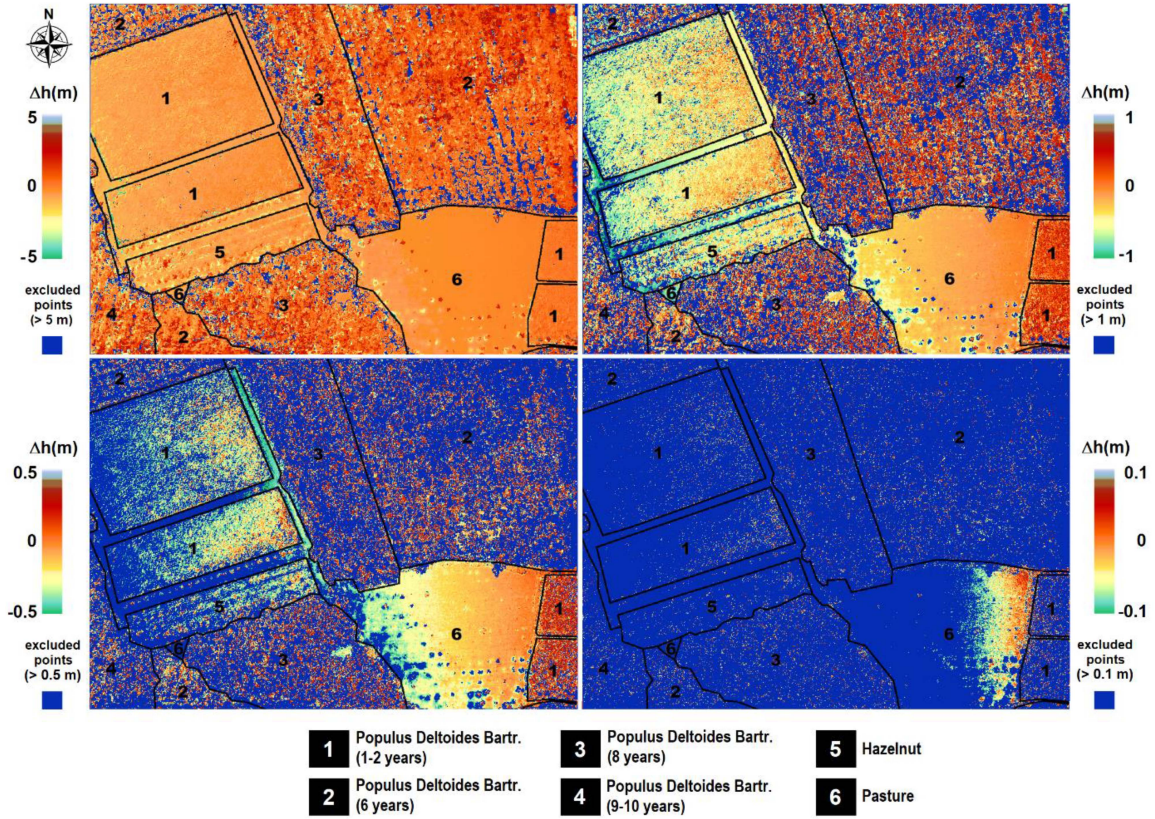
Fig. 9. DIFFDSMs of MS RTK and RGB non-RTK UAVs' DSMs for ± 5, ± 1, ± 0.5, and ± 0.1 m height difference scales.
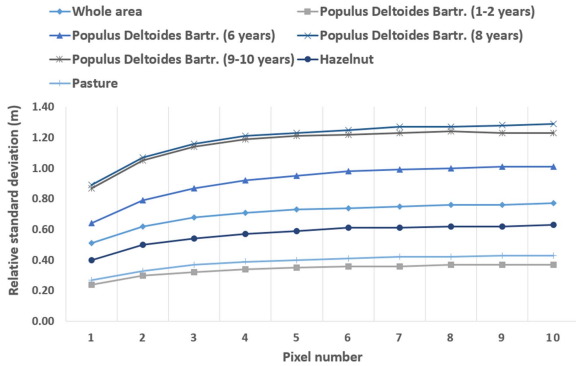

Fig. 10. Relative vertical consistency between MS RTK and RGB non-RTK UAVs' DSMs as RSZ.

of vegetation classes on the consistency was determined clearly

$$\text{DIFFDSM} = \text{DSM}_{\text{RTK}} - \text{DSM}_{\text{non-RTK}}. \qquad (12)$$

For demonstrating the relative vertical consistency between neighbor pixels on generated DSMs, relative standard deviation (RSZ) was calculated according to (13). In the equation, D describes the distance groups and D_l and D_u are the lower and upper range of the group. DZ_i and DZ_j are closely neighbored height points. In the RSZ analysis, 1st–10th pixel neighborhood

of each pixel was applied (point spacing $\times$ 10)

$$\text{RSZ} = \sqrt{\frac{\sum (DZ_i - DZ_j)^2}{2 \times n_v}}, D_l < D < D_u \qquad (13)$$

where n_v is the number of point combinations in the distance group. For the normalization of RSZ to SZ, multiplication factor of 2 for n_v was utilized. According to the error propagation, if the height differences of the neighboured points are independent, the RSZ would be the square root of 2.0 larger than SZ, described by $2 \times n_v$.

IV. RESULTS

The significant effect of filtering on the number and height interval of generated MS RTK and RGB non-RTK dense point clouds is shown in Table IV. Because of applying the elevation datum as orthometric in the analysis (also in Table IV), the ellipsoidal heights of the MS RTK UAV were undulated as 38.37 m. By means of higher spatial resolution (20 MP), the number of points in RGB UAV cloud is much more than MS RTK UAV data. However, approx. 8 million points in MS UAV cloud are strongly sufficient for 3D description of the study area. In Table IV, the significance of the detailed filtering is clearly seen. The simple filtering process of Agisoft Metashape is insufficient, particularly in vegetated, watery, and inclined topographic conditions, and detailed filtering is mandatory to

TABLE VI
ABSOLUTE VERTICAL CONSISTENCY BETWEEN GENERATED DSMs (α = TERRAIN INCLINATION)

Ref. DSM	Test DSM	Land Cover Class	Bias (m)	SZ (m)		NMAD (m)		KURTOSIS (m)		SKEWNESS (m)		Excluded Points (>5m) (%)
				SZ	SZ	NMAD	NMAD		$\alpha < 6°$		$\alpha < 6°$	
RGB	MS	Whole area (100%)	0.19	0.69+0.2×tan(α)	0.71	0.34+0.3×tan(α)	0.21	1.60	3.22	0.63	-0.14	3.02
			0.00	0.72+0.1×tan(α)	0.72	0.49+0.2×tan(α)	0.21	1.74	3.33	0.82	0.17	2.98
		Populus Deltoides Bartr. (1-2 years old) (20.84%)	-0.16	0.44+0.1×tan(α)	0.66	0.37+0.1×tan(α)	0.27	8.99	6.28	1.40	1.88	0.34
			0.00	0.40+0.1×tan(α)	0.64	0.26+0.1×tan(α)	0.27	8.27	6.02	1.16	1.74	0.34
		Populus Deltoides Bartr. (6 years old) (30.02%)	0.87	1.31+0.0×tan(α)	1.19	1.13+0.1×tan(α)	0.68	0.80	0.67	-0.42	-0.77	6.90
			0.00	1.04+0.0×tan(α)	1.27	0.80+0.0×tan(α)	0.87	0.60	-0.09	0.44	0.50	6.55
		Populus Deltoides Bartr. (8 years old) (21.54%)	0.73	1.43+0.0×tan(α)	1.36	1.11+0.0×tan(α)	0.88	0.62	0.15	-0.53	-0.44	6.34
			0.00	1.24+0.0×tan(α)	1.42	0.89+0.0×tan(α)	0.97	0.16	-0.14	0.34	0.43	5.96
		Populus Deltoides Bartr. (9-10 years old) (4.74%)	-0.28	1.35+0.0×tan(α)	1.43	1.25+0.0×tan(α)	1.27	-0.18	-0.34	0.51	0.75	8.33
			0.00	1.28+0.0×tan(α)	1.40	1.09+0.0×tan(α)	1.16	-0.32	-0.50	0.25	0.48	8.32
		Hazelnut (5.27%)	-0.24	0.71+0.0×tan(α)	1.13	0.54+0.0×tan(α)	0.49	3.99	1.17	0.86	0.85	2.00
			0.00	0.67+0.0×tan(α)	1.11	0.34+0.0×tan(α)	0.48	3.72	1.10	0.62	0.57	2.02
		Pasture (17.59%)	-0.10	0.54+0.21×tan(α)	0.34	0.18+0.43×tan(α)	0.16	11.01	12.17	-0.65	-1.35	0.84
			0.00	0.53+0.23×tan(α)	0.34	0.16+0.43×tan(α)	0.16	11.15	12.70	-0.83	-1.50	0.83

avoid the generation of misleading DSMs. As placed in Table IV, while the height intervals of MS RTK and RGB non-RTK UAVs are incompatible before detailed filtering, they reached cm level consistency with the effect of filtering.

The calculated and eliminated horizontal offsets in X and Y directions between MS RTK and RGB non-RTK UAVs' DSMs are shown in Table V. The offsets are around -0.7 pixel in X direction and $+0.4$ pixel in Y direction. Due to being under a pixel in both directions, the horizontal consistency of MS RTK and RGB non-RTK UAVs' DSMs was interpreted as high. The horizontal consistency results demonstrated that the planimetric positioning performance of onboard RTK GNSS receiver in vegetated areas is sufficient (<1 pixel).

Fig. 6 shows the generated DSMs in 0.25 m grid using MS RTK and RGB non-RTK UAVs' data. Although the values in height scales are similar, the description of the objects in RGB non-RTK UAV DSM looks more detailed. That means, the influence of the interpolation in vegetated terrain is different for MS RTK and RGB non-RTK UAVs' dense point clouds.

The absolute vertical consistencies of the DSMs for whole and uninclined areas in six vegetation classes were shown in Table VI. The uninclined areas were defined with $\arctan^{-1} 0.1$ which means ~6°. The analyses were performed considering systematic bias in two iterations as "with bias" and "without bias." The detected bias in the first iteration was eliminated in the second iteration. After bias elimination, the SZ and NMAD for the whole area were calculated as ± 0.72 and ± 0.49 m, respectively. While SZ values were detected as similar for whole and uninclined areas, absolute vertical consistency as NMAD was much higher in uninclined areas. This case proved the dominancy of minor outliers which hindered SZ to increase in that areas. The class analyses demonstrated that the elevation of the vegetation type directly effects the absolute vertical consistency of the DSMs. In Pasture, Hazelnut and Populus Deltoides Bartr. (1–2 years old) classes which have shorter elevation, the SZ and NMAD are between ± 0.4 and ± 0.67 m and ± 0.16 and ± 0.34 m, respectively. However, the SZ and NMAD rise up to ± 1.28 and ± 1.09 m, respectively, for the tallest Populus Deltoides Bartr. (9–10 years old) class. In addition, the increase in the percentage

of the excluded points in parallel with the rising elevation of the classes was observed. In shorter elevation classes such as Pasture, Hazelnut, and Populus Deltoides Bartr. (1–2 years old), kurtosis values are also reaching maximum levels because of the upward peak of the FDZ in comparison with normal distribution (please see Fig. 7).

Figs. 7 and 8 show the distribution of height differences between MS RTK and RGB non-RTK UAVs' DSMs as the FDZ, SZ, and NMAD separately for the whole area and uninclined area. In both figures, NMAD has higher consistency with FDZ and the mode of NMAD is around zero for Populus Deltoides Bartr. (1–2 years old), Hazelnut, and Pasture classes which have shorter elevation than other classes. In Figs. 7 and 8, the negative effect of minor outliers on SZ was also detected, and even ±2 m range was insufficient to represent the differences of all corresponding pixels. In Fig. 7, although normal distribution of height differences, which means a symmetric distribution, was observed in most classes, particularly FDZ values have an abnormal trend in Populus Deltoides Bartr. (9–10 years old) class ("e" in the histograms) due to the tallest elevations. In Fig. 8, due to very low number of uninclined pixels in Populus Deltoides Bartr. (6 years old), Populus Deltoides Bartr. (8 years old), Populus Deltoides Bartr. (9–10 years old), and hazelnut classes (c, d, e, and f in Fig. 8), the trends of the FDZ values were also monitored as abnormal.

The DIFFDSMs, facilitate the visual interpretation of height inconsistencies between the DSMs by detecting erroneous regions, are presented in Fig. 9. The DIFFDSMs were generated in four different scales as ±5, ±1, ±0.5, and ±0.1 m, and the vector plots of the vegetation classes were overlapped to clearly show the consistency level of RTK and non-RTK UAVs' DSMs. The blue regions in DIFFDSMs indicate excluded points that are out of range, determined. If the ±0.1 m scaled DIFFDSM is examined, it can be seen that there are only a limited number of points in the Pasture class (class 6 in Fig. 9). When the scale rises up to ±0.5 m, considerable parts of Populus Deltoides Bartr. (1–2 years old) and hazelnut classes were included in the DIFFDSM along with the Pasture class. About half of the Populus Deltoides Bartr. (6 years old), Populus Deltoides Bartr. (8 years old), and Populus Deltoides Bartr. (9–10 years old) classes were scarcely represented in ±1 m scale DIFFDSM. At the scale of ±5 m, almost all pixels from these three classes were included and only blunder points resulted in a very low number of gaps. This finding once again revealed why the maximum height difference of ±5 m between the DSM pixels compared with the reference was chosen when determining the excluded points. The DIFFDSM results clearly demonstrated that the performance of the on-board RTK GNSS positioning decreases with the rise of vegetation elevation.

The results of relative vertical consistency between MS RTK and RGB non-RTK UAVs' DSMs as RSZ are shown in Fig. 10. First, it should be pointed out that the RSZ results are coherent with the SZ and a little bit better. That means, the consistency between neighbor pixels is a little bit higher than the consistency of the whole model which indicates an interior intendancy of MS RTK DSM. First, it should be noted that the trends of the RSZ of all vegetation classes are similar. The Populus Deltoides Bartr. (1–2 years old) and the Pasture classes have the best and very

close RSZ values and the hazelnut class follows them. While Populus Deltoides Bartr. (6 years old) has a mean RSZ value, Populus Deltoides Bartr. (8 years old) and Populus Deltoides Bartr. (9–10 years old) classes have the worst RSZ values in a similar trend. Eventually, RSZ values promote that the rising elevation of the vegetation class directly influences the potential of on-board RTK GNSS receiver in MS UAV.

V. CONCLUSION

In the study, the horizontal and vertical consistency of MS RTK and RGB non-RTK UAVs' DSMs were analyzed in vegetated areas. The spectral difference between MS and RGB data was eliminated by using only the RGB band of MS UAV aerial photos in photogrammetric processing and DSM generation. The results showed that the horizontal positioning performance of on-board RTK GNSS receiver is sufficient and inconsistency is around 0.015 m in X and 0.008 m in Y directions. However, the results demonstrated considerable inconsistencies in the vertical positioning of analyzed DSMs. The results of both visual and statistical analyses promote that the most significant parameter which effects the vertical positioning performance of the on-board RTK GNSS receiver of the UAVs is the elevation of vegetation classes. While the MS RTK and RGB non-RTK UAVs' DSMs have ≤0.67 m as SZ and ≤0.34 m as NMAD consistency in shorter elevation Populus Deltoides Bartr. (1–2 years old), Hazelnut, and Pasture classes, SZ and NMAD reach up to ±1.28 and ±1.09 m, respectively, for the tallest Populus Deltoides Bartr. (9–10 years old) class. FDZ, SZ, and NMAD relations in whole and uninclined areas separately, multi-scale generated DIFFDSMs, and relative vertical consistency analyses have also confirmed the influence of the vegetation elevation in vertical quality decrease in the DSMs.

Overall, the results demonstrated that the lack of GCP-supported absolute orientation can cause serious problems in vertical representation quality of DSMs derived from RTK GNSS-equipped UAVs' aerial photos. According to these results, RTK GNSS-equipped UAV users should establish at least a few number of GCPs in the vegetated areas to provide a precise absolute orientation and high-quality DSM generation.

REFERENCES

[1] A. Kretov, V. Glukhov, and A. Tikhonov, "Conceptual assessment of the possibility of using cryogenic fuel on unmanned aerial vehicles," *Drones*, vol. 6, no. 8, Aug. 2022, Art. no. 217, doi: 10.3390/drones6080217.

[2] S. Chen, D. F. Laefer, and E. Mangina, "State of technology review of civilian UAVs," *Recent Patents Eng.*, vol. 10, no. 3, pp. 160–174, Dec. 2016, doi: 10.2174/1872212110666160712230039.

[3] G. Udeanu, A. Dobrescu, and M. Oltean, "Unmanned aerial vehicle in military operations," *Sci. Res. Educ. Air Force*, vol. 18, no. 1, pp. 199–206, 2016, doi: 10.19062/2247-3173.2016.18.1.26.

[4] L. I. N. Zongjian, "UAV for mapping—Low altitude photogrammetric survey," in *Proc. XXIst ISPRS Congr.*, 2008, vol. 37, no. B1, pp. 1183–1186.

[5] M. Pepe and D. Constantino, "UAV photogrammetry and 3D modelling of complex architecture for maintenance purposes: The case study of the masonry bridge on the Sele River, Italy," *Periodica Polytechnica Civil Eng.*, vol. 65, no. 1, pp. 191–203, Oct. 2021, doi: 10.3311/PPci.16398.

[6] D. Popescu, F. Stoican, G. Stamatescu, L. Ichim, and C. Dragana, "Advanced UAV–WSN system for intelligent monitoring in precision agriculture," *Sensors*, vol. 20, no. 3, Feb. 2020, Art. no. 817, doi: 10.3390/s20030817.

[7] C. Thiel and C. Schmullius, "Comparison of UAV photograph-based and airborne lidar-based point clouds over the forest from a forestry application perspective," *Int. J. Remote Sens.*, vol. 38, no. 8–10, pp. 2411–2426, 2017, doi: 10.1080/01431161.2016.1225181.

[8] J. Xiang, J. Chen, G. Sofia, Y. Tian, and P. Tarolli, "Open-pit mine geomorphic changes analysis using multi-temporal UAV survey," *Environ. Earth Sci.*, vol. 77, no. 6, pp. 1–18, Mar. 2018, doi: 10.1007/s12665-018-7383-9.

[9] S. P. Bemis et al., "Ground-based and UAV-Based photogrammetry: A multi-scale, high-resolution mapping tool for structural geology and paleoseismology," *J. Struct. Geol.*, vol. 69, no. A, pp. 163–178, Dec. 2014, doi: 10.1016/j.jsg.2014.10.007.

[10] F. J. Mesas-Carrascosa, M. D. Notario García, J. E. Meroño de Larriva, and A. García-Ferrer, "An analysis of the influence of flight parameters in the generation of unmanned aerial vehicle (UAV) orthomosaicks to survey archaeological areas," *Sensors*, vol. 16, no. 11, Nov. 2016, Art. no. 1838, doi: 10.3390/s16111838.

[11] U. G. Sefercik, T. Kavzoglu, M. Nazar, C. Atalay, and M. Madak, "UAV-based 3D virtual tour creation," *Int. Arch. Photogramm. Remote Sens. Spatial Inf. Sci.*, vol. XLVI-4/W5-2021, pp. 493–499, 2021, doi: 10.5194/isprs-archives-XLVI-4-W5-2021-493-2021.

[12] O. S. Ahmed et al., "Hierarchical land cover and vegetation classification using multispectral data acquired from an unmanned aerial vehicle," *Int. J. Remote Sens.*, vol. 38, no. 8–10, pp. 2037–2052, Feb. 2017, doi: 10.1080/01431161.2017.1294781.

[13] U. G. Sefercik et al., "3D positioning accuracy and land cover classification performance of the UAVs: Case study of DJI phantom IV multispectral RTK," in *Proc. 42nd Asian Conf. Remote Sens.*, 2021, pp. 119–128.

[14] W. Stempfhuber and M. Buchholz, "A precise, low-cost RTK GNSS system for UAV applications," *Int. Arch. Photogrammetry, Remote Sens. Spatial Inf. Sci.*, vol. XXXVIII-1/C22, pp. 289–293, 2012, doi: 10.5194/isprsarchives-XXXVIII-1-C22-289-2011.

[15] M. Štroner, R. Urban, J. Seidl, T. Reindl, and J. Brouček, "Photogrammetry using UAV-mounted GNSS RTK: Georeferencing strategies without GCPs," *Remote Sens.*, vol. 13, no. 7, Mar. 2021, Art. no. 1336, doi: 10.3390/rs13071336.

[16] E. Remzi, E. Alkan, and A. Aydın, "A comparative analysis of UAV-RTK and UAV-PPK methods in mapping different surface types," *Eur. J. Forest Eng.*, vol. 7, no. 1, pp. 12–25, Jun. 2021, doi: 10.33904/ejfe.938067.

[17] O. Lewicka, M. Specht, and C. Specht, "Assessment of the steering precision of a UAV along the flight profiles using a GNSS RTK receiver," *Remote Sens.*, vol. 14, no. 23, Dec. 2022, Art. no. 6127, doi: 10.3390/rs14236127.

[18] K. Jacobsen, "Development of large area covering height model," *Int. Arch. Photogrammetry, Remote Sens. Spatial Inf. Sci.*, 2014, vol. XL, no. 4, pp. 105–110, doi: 10.15488/883.

[19] L. Iglesias, C. De Santos-Berbel, V. Pascual, and M. Castro, "Using small unmanned aerial vehicle in 3D modeling of highways with tree-covered roadsides to estimate sight distance," *Remote Sens.*, vol. 11, no. 22, Nov. 2019, Art. no. 2625, doi: 10.3390/rs11222625.

[20] U. G. Sefercik, F. Tanrikulu, and C. Atalay, "Comparison of photogrammetric 3D modeling potentials of SFM-based next generation image matching software," *Turkish Photogrammetry J.*, vol. 2, no. 2, pp. 39–45, Dec. 2020.

[21] M. J. Westoby, J. Brasington, N. F. Glasser, M. J. Hambrey, and J. M. Reynolds, "Structure-from-Motion'photogrammetry: A low-cost, effective tool for geoscience applications," *Geomorphology*, vol. 179, pp. 300–314, Dec. 2012, doi: 10.1016/j.geomorph.2012.08.021.

[22] U. G. Sefercik, F. Tanrikulu, and C. Atalay, "Photogrammetric 3D modelling potential comparison of SFM-based new generation image matching software," *Proc. 40th Asian Conf. Remote Sens.*, vol. 1, no. 8, pp. 1–8, 2019.

[23] E. Sanz-Ablanedo, J. H. Chandler, J. R. Rodríguez-Pérez, and C. Ordóñez, "Accuracy of unmanned aerial vehicle (UAV) and SfM photogrammetry survey as a function of the number and location of ground control points used," *Remote Sens.*, vol. 10, no. 10, 2018, Art. no. 1606, doi: 10.3390/rs10101606.

[24] C. Stöcker, F. Nex, M. Koeva, and M. Gerke, "Quality assessment of combined IMU/GNSS data for direct georeferencing in the context of UAV-based mapping," *Int. Arch. Photogrammetry, Remote Sens. Spatial Inf. Sci.*, vol. 42, pp. 355–361, 2017, doi: 10.5194/isprs-archives-XLII-2-W6-355-2017.

[25] M. Rabah, M. Basiouny, E. Ghanem, and A. Elhadary, "Using RTK and VRS in direct geo-referencing of the UAV imagery," *Nriag J. Astron. Geophys.*, vol. 7, no. 2, pp. pp. 220–226, 2018, doi: 10.1016/j.nrjag.2018.05.003.

[26] W. T. Tinkham and N. C. Swayze, "Influence of agisoft metashape parameters on UAS structure from motion individual tree detection from canopy height models," *Forests*, vol. 12, no. 2, Feb. 2021, Art. no. 250, doi: 10.3390/f12020250.

[27] A. A. Teixeira, C. W. Mendes Júnior, C. Bredemeier, M. Negreiros, and R. D. S. Aquino, "Evaluation of the radiometric accuracy of images obtained by a sequoia multispectral camera," *Engenharia Agrícola*, vol. 40, no. 6, pp. 759–768, Nov./Dec. 2020, doi: 10.1590/1809-4430-Eng.Agric.v40n6p759-768/2020.

[28] M. Hollaus, G. Mandlburger, N. Pfeifer, and W. Mücke, "Land cover dependent derivation of digital surface models from airborne laser scanning data," *Int. Arch. Photogrammetry, Remote Sens. Spatial Inf. Sci.*, vol. XXXVIII, no. 3A, pp. 221–226, 2010.

[29] C. S. Yang, S. P. Kao, F. B. Lee, and P. S. Hung, "Twelve different interpolation methods: A case study of surfer 8.0," in *Proc. XXth ISPRS Congr.*, 2004, pp. 778–785.

[30] E. Baltsavias, A. Gruen, H. Eisenbeiss, L. Zhang, and T. Waser, "High-quality image matching and automated generation of 3D tree models," *Int. J. Remote Sens.*, vol. 29, no. 5, pp. 1243–1259, Feb. 2008, doi: 10.1080/01431160701736513.

[31] J. M. Hellerstein, "Quantitative data cleaning for large databases," Tech. Rep., United Nations Economic Commission for Europe (UNECE), 2008.

Umut Gunes Sefercik was born in Türkiye on February 17, 1981. He received the B.Sc. degree in application of edge detection techniques on stratigraphic structures from the Department of Geomatics Engineering, Zonguldak Bulent Ecevit University, Zonguldak, Türkiye, in 2003, the M.Sc. and Ph.D. degrees in DEM generation and validation from SRTM and TerraSAR-X satellite SAR data from Zonguldak Bulent Ecevit University, Zonguldak, Türkiye, in 2006 and 2010, respectively.

During M.Sc. and Ph.D. degrees, he continued his thesis studies in the Institute of Photogrammetry and Geoinformation, Leibniz University of Hannover, Germany, as a research scholar. He finished his postdoctoral research between 2013 and 2014 with National Centre for Airborne Laser Mapping (NCALM), University of Houston, Houston, TX, USA. He started his career with his own mapping company in 2003 and passed to the Zonguldak Bulent Ecevit University, Geomatics Engineering Department as a research assistant in 2005. Since 2020, he has been working as an academic staff (Prof. Dr.) with the Department of Geomatics Engineering, Gebze Technical University, Türkiye. He has more than 20 projects, 30 indexed journal papers, 3 book chapters, 55 international proceedings, and more than 20 national proceedings about his specialization areas. He has completed nearly 200 reviews for 42 international journals and has worked as an editorial board member in 4 international journals. His research interests include generation and quality validation of 3D map products using remote sensing technologies such as unmanned aerial vehicle, airborne laser scanning, synthetic aperture radar, and digital photogrammetry.

Dr. Sefercik is currently a member of International Society for Photogrammetry and Remote Sensing and International Society for Digital Earth.

Mertcan Nazar was born in Türkiye, on September 15, 1996. He received the B.Sc. degree in maximum likelihood pixel-based classification in UAV orthomosaics from the Department of Geomatics Engineering, Istanbul Technical University, Istanbul, Türkiye, in 2020, the M.Sc. degree in generation of precise UAV 3D models and integration them to game engines in 2022, from the Department of Geomatics Engineering, Gebze Technical University (GTU), Darıca, Türkiye, where he is currently working toward the Ph.D. degree in automatic risk mapping on power transmission lines with UAV Lidar technology with the Department of Geomatics Engineering.

Since 2020, he is a Research Assistant with Geomatics Engineering Department, GTU. He has more than 10 indexed journal papers and international proceedings. His research interests include mapping with unmanned aerial vehicle and airborne laser scanning technologies, fuzzy logic, and data integration to the virtual environment.